



# Effect of blade leading-edge microcylinder in a Wells turbine used for wave energy converters

P. Sadees<sup>1</sup> · P. Madhan Kumar<sup>2</sup> · Abdus Samad<sup>1</sup>

Received: 12 July 2022 / Accepted: 27 December 2022 / Published online: 30 January 2023  
© The Author(s), under exclusive licence to Springer Nature Switzerland AG 2023

## Abstract

The present study attempts to enhance a Wells turbine performance by adopting a leading-edge microcylinder (LEM) as a passive flow control device. The microcylinder is placed near the blade leading edge so that its axis lies on the chord line of the rotor blade. The influence of turbine performance, due to parameters such as microcylinder diameter and the distance between the cylinder and the blade leading edge, is evaluated by solving the steady Reynolds-averaged Navier–Stoke (RANS) equations with the  $k-\omega$  SST turbulence model. The performance parameters of the microcylinder rotor were compared with the reference rotor. It was found that the pair of counter-rotating and co-rotating vortices shed from the microcylinder feed kinetic energy to the separated flow and re-energize the boundary layer. This phenomenon delays the flow separation and enhances the operating range. Moreover, a parametric investigation of the microcylinder rotor reveals that the diameter and space between the microcylinder and the rotor blade are instrumental in delaying flow separation. It was found that a cylinder diameter equal to  $0.02C$  ( $C$  is blade chord) and a distance between the leading edge and the micro cylinder equal to  $0.035C$  resulted in increases in the working range and in the average torque equal to about 22% and 49%, respectively.

**Keywords** Passive flow control · Leading-edge microcylinder · Wells turbine · OWC · WEC

## Abbreviations

BLR	Baseline rotor
HCV	Hub corner vortex
HPR	High-performance rotor
LE	Leading-edge
LEVG	Leading-edge vortex generator
LEM	Leading-edge microcylinder
PL	Profile loss
PS	Pressure surface
RANS	Reynolds-averaged Navier–Stokes
SFL	Secondary flow loss

SS	Suction surface
SST	Shear stress transport
TKE	Turbulent kinetic energy
TLF	Tip leakage flow
TLV	Tip leakage vortex

## Symbols

$C$	Chord length ( $m$ )
$C_f = \frac{\tau_w}{0.5\rho U_A^2}$	Skin friction coefficient (–)
$C_p$	Static pressure drop coefficient (–)
$C_{ptot} = \frac{p_1 - p_2}{0.5\rho U_A^2}$	Total pressure loss coefficient (–)
$D$	Diameter of the microcylinder ( $m$ )
$D_{tip}$	Tip diameter ( $m$ )
$h = \frac{R_{hub}}{R_{tip}}$	Hub-to-tip ratio (–)
$K$	Specific turbulent kinetic energy ( $m^2/s^2$ )
$l$	The gap between microcylinder center and blade LE ( $m$ )
$p_1$	Stagnation pressure at the inlet ( $Pa$ )
$p_2$	Stagnation pressure at the outlet ( $Pa$ )
$Q$	Airflow rate ( $m^3/s$ )

✉ Abdus Samad  
samad@iitm.ac.in

P. Sadees  
pg.sadees@gmail.com

P. Madhan Kumar  
madyypts@gmail.com

<sup>1</sup> Wave Energy and Fluids Engineering Laboratory, Indian Institute of Technology Madras, Chennai 600036, India

<sup>2</sup> LHEEA, CNRS UMR 6598, Centrale Nantes, 1 Rue de La Noë, BP 92101, 44321 Nantes Cedex 3, France

$R_{hub}$	Hub radius ( $m$ )
$R_{tip}$	Tip radius ( $m$ )
$T_t$	Total torque ( $N.m$ )
$U_A$	Inlet axial velocity ( $m/s$ )
$U_{tip}$	Rotor tip velocity ( $m/s$ )
$V_a^*$	Non-dimensional axial velocity (–)
$V_c^*$	Non-dimensional circumferential velocity (–)
$z^*$	Normalized span (–)
$E$	Dissipation rate ( $m^2/s^3$ )
$P$	The density of air ( $kg/m^3$ )
$\Omega$	Rotational speed ( $rpm$ )
$\Omega$	Specific turbulent dissipation rate ( $s^{-1}$ )
$\tau_w$	Wall shear stress ( $Pa$ )
$\omega_z^*$	Normalized $z$ -vorticity (–)
$\Delta p$	Static pressure drop ( $Pa$ )
$T^*$	Torque coefficient (–)
$U^*$	Flow coefficient (–)
$\Delta p^*$	Static pressure drop coefficient (–)
$\eta$	Efficiency (%)

## 1 Introduction

The ocean is one of the renewable energy sources that can be harvested using suitable methods to fulfil growing human energy demands. These sources are non-depleting and have minimal harmful environmental effects compared to fossil fuel-based energy sources. Recent decades have seen tremendous research and development in harnessing ocean energy like wave energy converters (WECs). WEC aims at converting the energy in the waves to electrical energy. Numerous efforts have been made to develop a commercially viable wave energy device (Falcao 2010) and improve the performance of various WEC devices, including an oscillating water column (OWC), overtopping, point absorbers, oscillating wave surge converters, and many others. The OWC, owing to its simplicity of operation, is one of the widely studied WEC devices (Shalby et al. 2019). It comprises an air chamber and a submerged water column. This oscillating airflow rotates an air turbine is coupled with a generator to produce electrical energy.

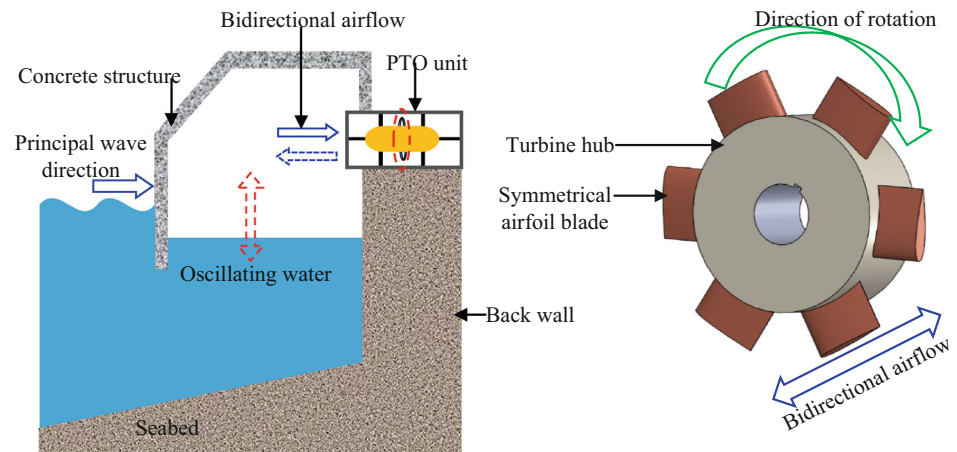
Among several types of turbines, a commonly used turbine is a reaction turbine known as Wells turbine. It is an axial flow turbine (Fig. 1) with a symmetric airfoil profile and  $90^\circ$  stagger angle. The turbine is self-rectifying and rotates in a single direction, regardless of the direction of incoming airflow. However, it has several drawbacks: poor starting capabilities, a higher noise level during the operation, and a limited operating range (Ragunathan 1995). Various design parameters were modified and reported by several

researchers (Shehata et al. 2017a). The main aim is to reduce turbomachinery losses (profile loss, end wall loss, and flow leakage loss). Hence, the concept of active and passive flow control comes into the picture. In the active flow control technique, the momentum and induced kinetic energy (supplied by additional components) regulate the flow separation and provide a wide range of operations. In this technique, a secondary energy source is always required, which makes the system more complex or energy consuming (Donovan et al. 1998; Buchmann et al. 2013; Yahiaoui et al. 2015; Greenblatt et al. 2021). In this paper, one of the passive flow control mechanisms is adopted, which will be discussed later in this section. On-surface and off-surface modification techniques were implemented for flow modifications.

There are ample research works available for on-surface modifications. A blade with a positive pitch angle creates a system with higher mean efficiency for each wave cycle (Kim et al. 2003). The variable chord blade alters the axial flow velocity of the turbine to increase efficiency. Several on-surface modifications were reported (Cui and Hyun 2016; Halder et al. 2017; Shehata et al. 2017b; Kumar et al. 2018, 2021; Nazeryan and Lakzian 2018), and they controlled the flow separation effectively by this method. Tip leakage flow (TLF) interacts with passage flow and promotes separation. Hence, reducing the TLF can assist turbine performance (Halder et al. 2017; Kumar et al. 2018, 2021) (Here, the separation implies low blade loading and low energy transfer to the blade and generates low torque to the turbine.) Numerous studies on the Wells turbine TLF have shown that improvements to the casing or lower tip gaps can increase performance (Cui and Hyun 2016).

Takao et al. (2000) stated that the three-dimensional guide vanes altered flow behavior more effectively than the two-dimensional guide vanes and reduced the angle of attack (AOA) around the hub of the blade, enhancing the turbine operating range. The tip clearance parameter indicates a possible impact on the effectiveness of the Wells turbine. A high tip clearance produced a lower peak efficiency and a wider stall margin, and a lower tip clearance produced a higher peak efficiency and stall margin (Watterson and Ragunathan 1997). According to Taha et al. (2011), a non-uniform tip clearance has a wider operating range. The casing groove lowers the intensity of TLF and mainstream flow interaction and improves stall margin and non-dimensional torque (Halder et al. 2015).

The airfoil leading-edge (LE) modification was used for various applications. The primary goal of the LE modification was to improve the aerodynamic performance of the airfoil in its intended application. The Krueger-type flap provides a higher lift and reduces an aircraft's 4–7% fuel burn rate (Strüber and Wild 2014). Beyhaghi and Amano (2017) studied a LE span-wise slot as a passive flow controller to enhance the lift coefficient in the NACA 4412 airfoil. Stough

**Fig. 1** Schematic view of OWC with Wells turbine

et al. (1985) demonstrated that the LE droop enhanced the aircraft's spin resistance and delayed the stall onset. Stall fences increase stall margin (Das and Samad 2020). Kumar and Govardhan (2011) implemented a stream-wise end wall fence to mitigate secondary flow losses. The LE protuberance induces a circulation gradient which causes the pre-stall separation and post-stall attachment in the flow field (Cai et al. 2019). Hansen et al. (2011) analyzed multiple combinations of amplitude and wavelength of the LE tubercles in the NACA 65-021 and the NACA 0021 airfoils. The NACA 65-021 airfoil exhibited relatively better performance. Mai et al. (2008) adopted the leading-edge vortex generator (LEVG) to improve the OA 209 rotorcraft airfoil aerodynamic characteristics. The LEVG generated longitudinal vortices at higher incidences, which diminished the SS flow separation.

Although the concept mentioned above is applied to other turbines, it is not implemented for the Wells turbine (which works on sinusoidally varying flow). In addition, a cylinder placed in front of the LE proved beneficial in improving aerodynamic performance. Jacob et al. (2005) presented a LE cylinder–airfoil configuration as a benchmark experiment to predict broadband noise. Luo et al. (2017) reported that the size of the cylinder and the gap between the cylinder and LE were critical parameters. For better stalling behavior, essential parameters were optimized. According to Zhong et al. (2019), the cylinder enhanced the airfoil's lift by reducing flow separation and increasing tangential force and power coefficient. Gopalkrishnan et al. (1994) found that in a typical D-section cylinder for NACA0012 airfoil, the average efficiency of the airfoil strongly depends on the vortex strength created by the cylinder. Wang et al. (2018) stated that the installation of an appropriate leading-edge microcylinder (LEM) in front of the horizontal axis wind turbine blade LE provided adequate flow separation control and improved the torque output. A small cylinder improved the power coefficient (Mostafa et al. 2022). Recently, two studies have been

**Table 1** Turbine specifications

No of blades	8
Airfoil profile	NACA 0015
Chord length	125 mm
Tip radius	300 mm
Mean radius	250 mm
Hub-to-tip ratio	0.666
Solidity	0.64
Clearance	1.25 mm (Torresi et al. 2004, 2008; Shaaban and Hafiz 2012; Halder et al. 2015)
Rotation speed	2000 rpm

reported for the performance improvement of the Wells turbine with LEM. First, Sadees et al. (2021) reported that the chord-wise LEM enhanced the operating range of the Wells turbine by 11.11%. Later, Geng et al. (2021) reported optimization of the span-wise placement of LEM and concluded that the relative working range and peak torque increased by 19.15% and 26.57%, respectively.

The above studies show that the LEM is a passive flow control device to enhance aerodynamic performance. This article reports the effect of a LEM in a Wells turbine blade for a steady-state unidirectional flow. The problem was solved numerically for different LEM diameters ( $d = 0.5$  to  $2\% C$ ) and gaps ( $l = 1$  to  $5\% C$ ). The flow features were investigated and reported in the article.

## 2 Geometry definition of reference and modified case

In this work, a Wells turbine with eight blades was used. Table 1 shows the specifications of the baseline rotor (Torresi et al. 2008), and Fig. 2 shows the schematic representation. The reference geometry was created by SolidWorks 2019. A LEM

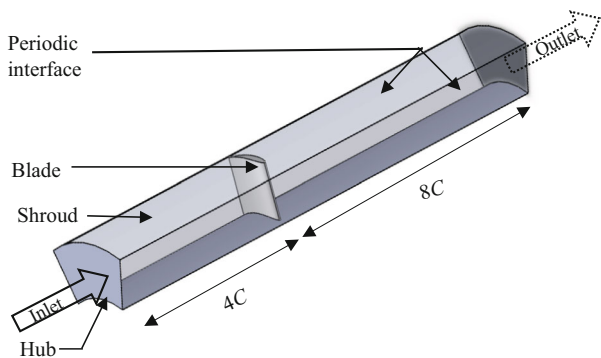


Fig. 2 Computational domain

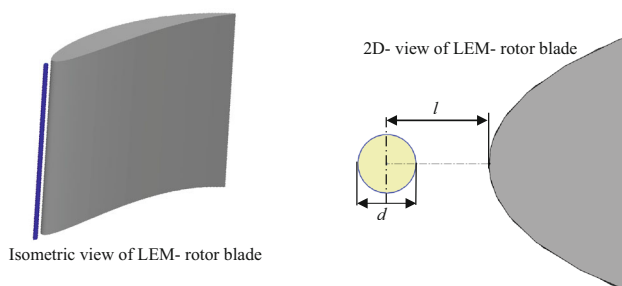


Fig. 3 Schematic view of modified LEM rotor blade

was added in front of the reference turbine in a chord-wise direction so that the blade symmetry was unaltered, as shown in Fig. 3. The design parameters  $l$  and  $d$  were varied in the range of  $1\%C$  to  $5\%C$  and  $0.5\%C$  to  $2\%C$  with steps of 0.5, respectively. The  $l$  and  $d$  bounds were chosen based on the design feasibility and their influence on the meshing process during the generation of prism layers around the cylinder and rotor blade.

The following performance parameters of the turbine were introduced,

$$T^* = \frac{T_t}{\rho_a \Omega^2 D_{tip}^5}, \Delta p^* = \frac{\Delta p}{\rho_a \Omega^2 D_{tip}^2}, \eta = \frac{T_t \Omega}{Q \Delta p}, U^* = \frac{U_A}{U_{tip}}$$

Here,  $T^*$  is torque coefficient,  $T_t$  is total torque (Nm),  $\rho_a$  is the density of air ( $kg/m^3$ ),  $\Omega$  is rotational speed (rpm),  $D_{tip}$  is tip diameter (m),  $\Delta p^*$  is pressure drop coefficient,  $\Delta p$  is stagnation pressure drop (Pa),  $\eta$  is efficiency, and  $Q$  is airflow rate ( $m^3/s$ ).

### 3 Computational methodology

The computational domain contained only one blade; the upstream and downstream domains were  $4C$  and  $8C$ . The

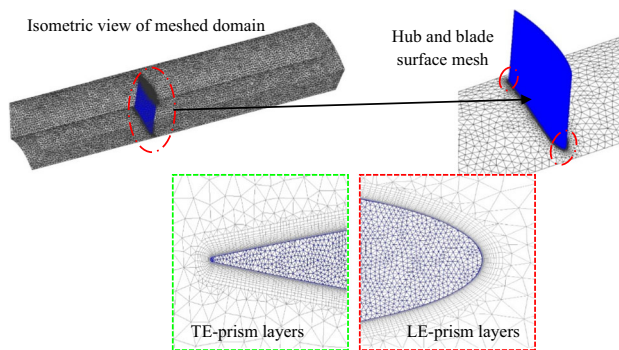


Fig. 4 Computational mesh

Table 2 Boundary conditions

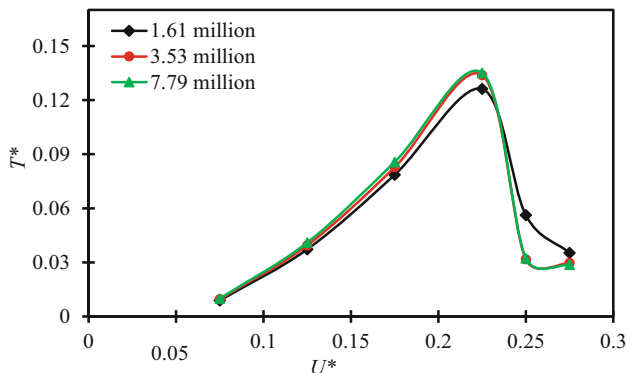
Working fluid	Air
Nature of flow	Incompressible
Computational domain	Single blade with a periodic interface
Inlet	Velocity inlet
Outlet	Pressure outlet
Blade, shroud, and hub	No-slip wall
Reference pressure	1 atm
Turbulence intensity	5%
Turbulence model	$k-\omega$ SST
Residual convergence criteria	$1 \times 10^{-5}$

unstructured tetrahedral elements were used to create the mesh in ICEM CFD (Fig. 4). Three-dimensional incompressible steady-state RANS equations were solved. Twenty prism layers were built around the blade and the cylinder to resolve the boundary layer with an exponential growth ratio of 1.2. The initial layer height was 0.01 mm to maintain  $y^+ < 1$ . The residual convergence criteria were fixed at  $10^{-5}$ , and the total number of iterations was 4000. The moving reference frame (MRF) method was adopted. The boundary conditions are shown in Table 2.

Based on the available literature, the  $k-\omega$  SST (Menter 1994) was chosen as the turbulence model in the present work to predict flow physics better. It was a hybrid model that switched between the  $k-\omega$  and  $k-\epsilon$  models for the near-wall and free-stream regions. The  $k-\omega$  SST model binds the standard  $k-\epsilon$  and  $k-\omega$  models, and these ( $\epsilon$  and  $\omega$ ) parameters are derived from the blending function. A second-order high-resolution advection scheme is used for spatial discretization. ANSYS CFX 18.1 computational fluid dynamics (CFD) code was used in this work. It is a fully implicit coupled solver that resolves the pressure and velocity equations concurrently. Compared to a segregated solver, the coupled solver decreases the number of iterations required to reach convergence (ANSYS-CFX 2011). The computational analysis was

**Table 3** GCI analysis

Number of elements ( $10^6$ )	$N_1, N_2, N_3$	7.79, 3.53, 1.61
Average grid size ( $h$ )	$h_1, h_2, h_3$	0.005043, 0.006564, 0.008536
Grid refinement factor ( $r$ )	$r_{21}, r_{32}$	1.3, 1.3
Critical parameter studied ( $\phi$ )	$\phi_1, \phi_2, \phi_3$	0.135064, 0.133836, 0.126194
Apparent order	$P$	6.8
Extrapolated values	$\phi_{ext}^{21}, \phi_{ext}^{32}$	0.135342, 0.135352
Approximation relative error (%)	$e_a^{21}, e_a^{32}$	0.93, 5.71
Extrapolated relative error (%)	$e_{ext}^{21}, e_{ext}^{32}$	0.18, 1.12
Grid convergence index (%)	$GCI_{fine}^{21}, GCI_{medium}^{32}$	0.23, 1.42

**Fig. 5** Grid independency study

carried out using the AQUA supercluster at the IIT Madras, Chennai, and the computational time of each simulation of 8–10 h is required.

## 4 Results and discussion

### 4.1 Grid independency test

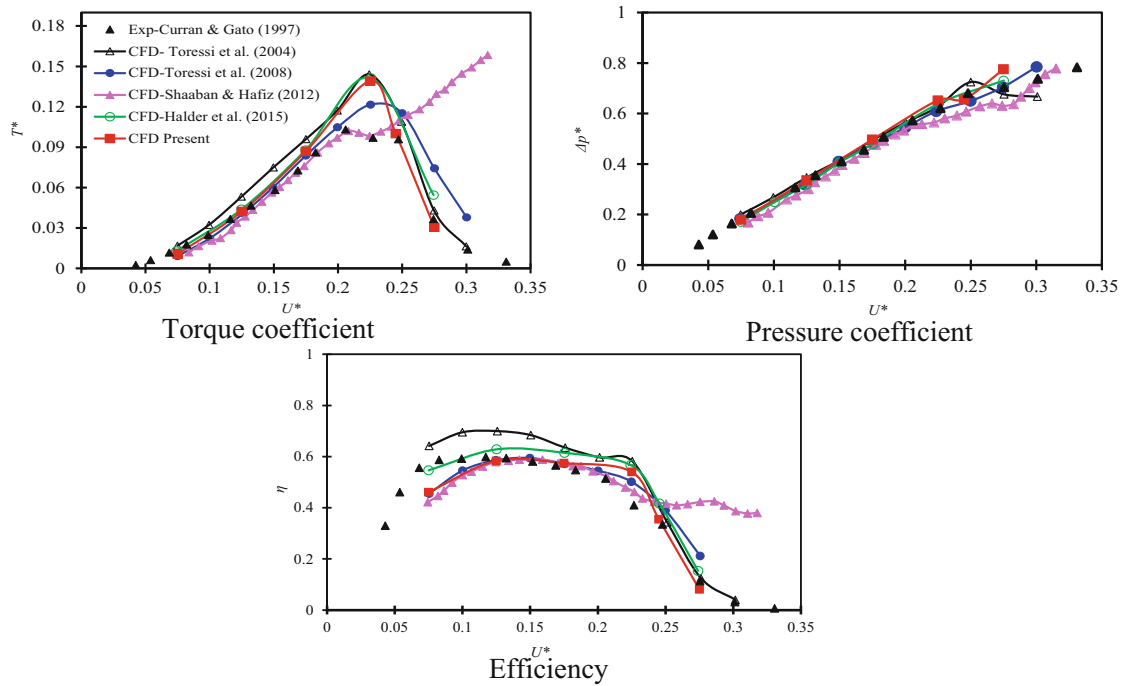
Table 3 shows the grid independency study for the reference blade geometry and the grid convergence index (GCI) for three grids (1.61 million coarse, 3.53 million medium, and 7.79 million fine). A consistent grid growth ratio was used for the successively refined grids to ensure uniform mesh refinement. According to Celik et al. (2008), the refinement factor was 1.3, and the torque coefficient was the critical performance parameter. The GCI decreases as the grid resolution increases, and the obtained fine and medium GCI were 0.23% and 1.42%. GCI was less than 2%, and the spatial grid convergence was reached in the medium grid. Hence, the medium grid was used for further analysis. Figure 5 shows that the torque variation is marginal with medium and fine grids.

### 4.2 Numerical validation

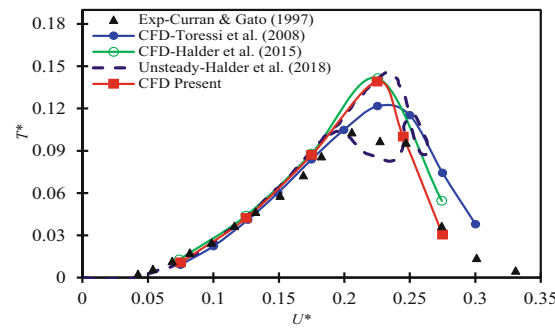
The numerical results were compared with the experimental results (Curran and Gato 1997) and steady-state numerical results (Torresi et al. 2004, 2008; Shaaban and Hafiz 2012; Halder et al. 2015). Figure 6a shows the dimensionless torque coefficient ( $T^*$ ), pressure drop coefficient ( $\Delta p^*$ ), and efficiency ( $\eta$ ) plotted against the flow coefficient ( $U^*$ ). The present CFD results match the existing results except those of Shaaban and Hafiz (2012). The work of Shaaban and Hafiz (2012) did not capture the stall; therefore, the performance parameters ( $T^*$  and  $\eta$ ) did not show a rapid drop. Various transient studies were performed on the Wells turbine to understand its unsteady flow behavior. They have reported that the dynamic effects of the Wells turbine are negligible because of a significantly lower value of reduced frequency (present case =  $6.25E-4$ ) (Ghisu et al. 2015, 2016, 2017). Furthermore, the unsteady results from the work of Halder et al. (2015) showed a marginal difference between the stall point of the steady and the unsteady cases (Fig. 6b). The prediction of stall point was similar for both the steady and unsteady results, and the present study used steady simulation to save the computational time. The present results slightly overestimate the torque at the stall point. Based on a better agreement with the existing data and accurate stall point prediction, it can be concluded that the current numerical model is adequate to study the Wells turbine rotor with a LEM.

### 4.3 Effect of cylinder diameter (d) and gap (l)

Table 4 represents the combined effect of the gap ( $l = 1\%$  to  $5\%C$ ) and the diameter ( $d = 0.5\%$  to  $2\%C$ ). Figure 7 (a–h) illustrates the cylinder effect for different flow coefficients ( $U^*$ ) with respective performance parameters such as  $T^*$ ,  $\Delta p^*$ , and  $\eta$ . The flow through a lower gap ( $l = 1\%C$ ) faces blockage and deteriorates the rotor performance due to kinetic energy losses in the incoming airflow. With a further increase in the gap, the rotor performance improves. As the value of  $l$  increases beyond the optimum value, the LEM



(a) Computational validation with existing results



(b) Comparison of steady and unsteady results of  $T^*$  with existing results.

**Fig. 6** (a) Computational validation with existing results. (b) Comparison of steady and unsteady results of  $T^*$  with existing results

**Table 4** Details on the stall margin percentage variance

Rotor type	Gap ( $l$ )	Diameter ( $d$ )			
		0.5% $C$	1% $C$	1.5% $C$	2% $C$
Case A	1% $C$	0	0	- 22.22%	-
Case B	1.5% $C$	11.11%	11.11%	11.11%	- 11.11%
Case C	2% $C$	11.11%	11.11%	22.22%	22.22%
Case D	2.5% $C$	11.11%	11.11%	11.11%	22.22%
Case E	3% $C$	0	11.11%	11.11%	22.22%
Case F	3.5% $C$	0	11.11%	11.11%	22.22%
Case G	5% $C$	- 22.22%	11.11%	11.11%	11.11%

**Fig. 7** Effects of LEM on Wells turbine performance

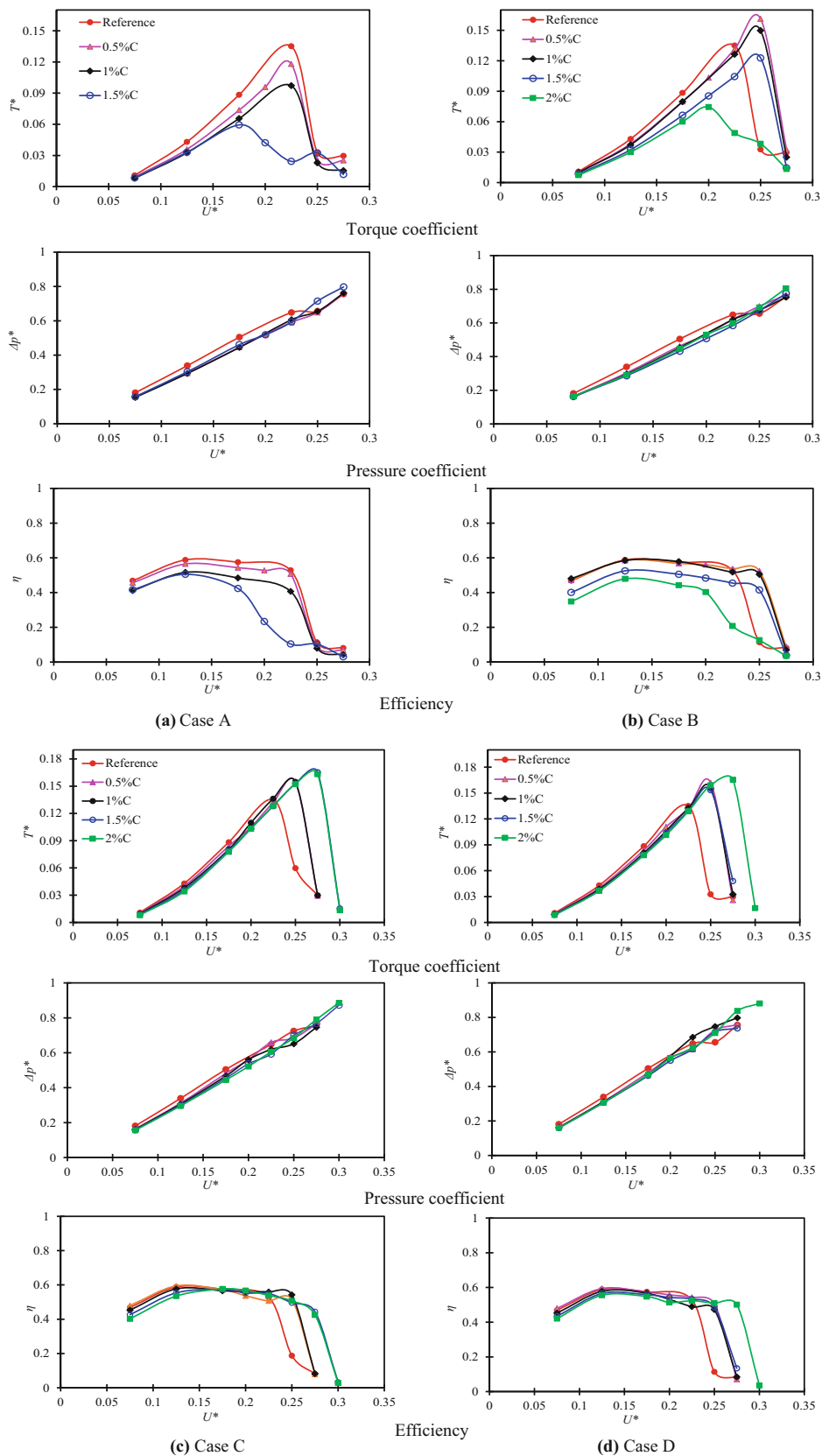
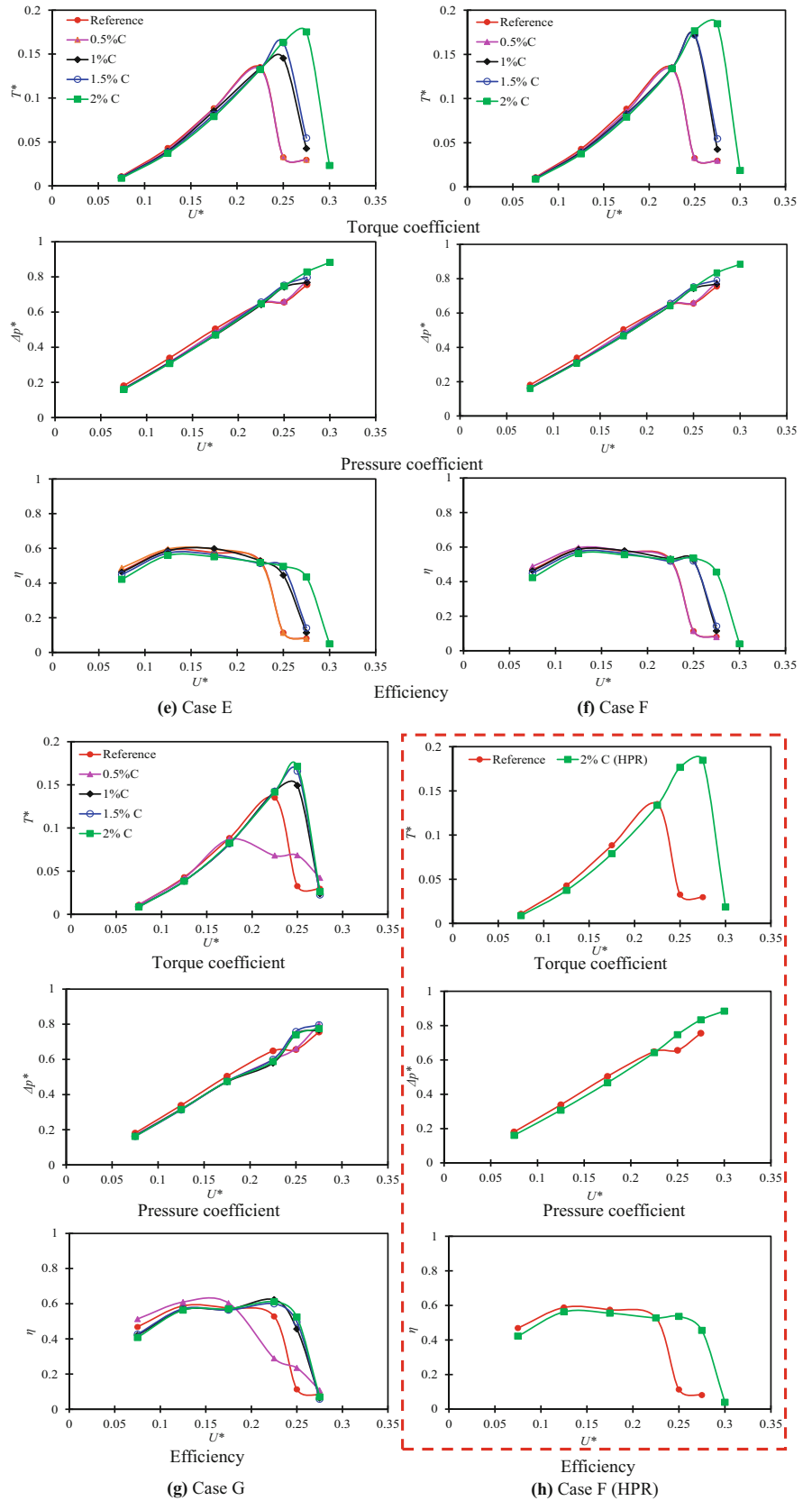
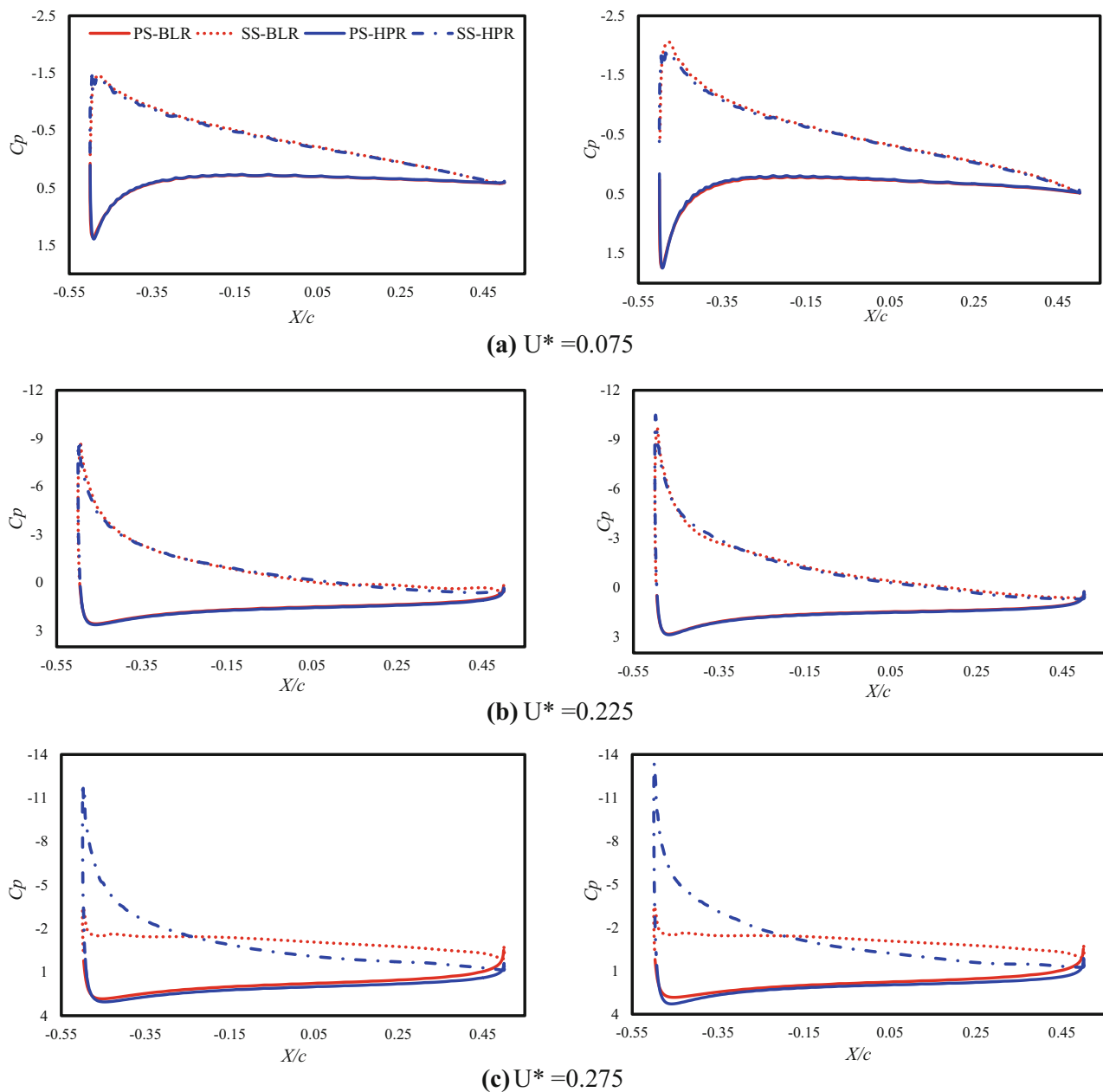


Fig. 7 continued





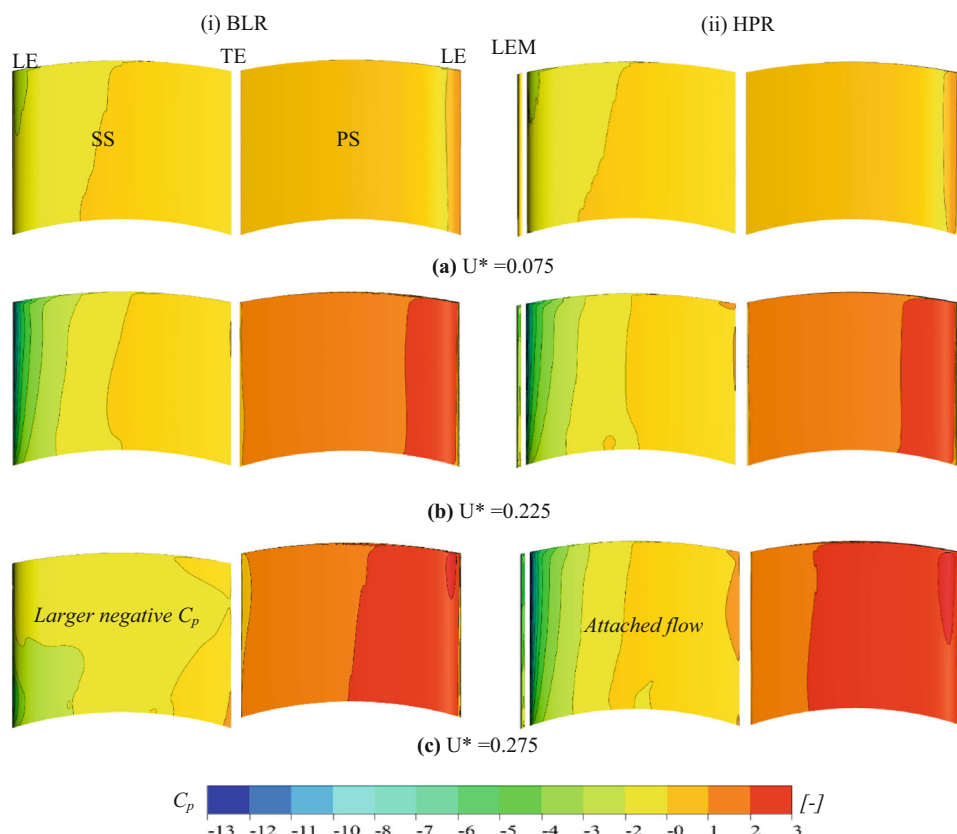


**Fig. 8** Pressure coefficient distribution at mid-span (right) and tip (left)

advantage diminishes due to increased momentum dissipation. A lower diameter ( $= 0.5\%C$ ) has a negligible impact and is similar to the baseline rotor (BLR) (Case A, E, and F). The enhanced kinetic energy transfer from the counter-rotating vortices to the boundary layer in the modified cases (Case B, C, and D) produces a higher stall margin (11.11%) for a lower  $d$  ( $= 0.5\%C$ ) (Table 4). A higher gap ( $= 5\%C$ ) and a lower diameter ( $= 0.5\%C$ ) facilitate lower flow obstruction, a lower strength vortex, increased kinetic energy losses in the incoming flow, and reduced rotor performance (Luo et al. 2017).

In addition,  $d = 1\%C$  shows a similar operating range at a lower gap ( $= 1\%C$ ) than the BLR case (Case A). In other cases (Cases B–G), the stall margin improves by 11.11% for the same diameter ( $= 1\%C$ ). A lower gap ( $= 1\%C$ ) and a higher diameter ( $= 1.5\%C$ ) increase blockage and reduce stall margin by 22.22% (Table. 4). Case C ( $l = 2\%C$  and  $d = 1.5\%C$  to  $2\%C$ ) and Cases D to F ( $d = 2\%C$  and  $l = 2.5$ – $3.5\%C$ ) enhanced the operating range by 22.22%. In Case F, the combination  $d = 2\%C$  and  $l = 3.5\%C$  in Case F produces a high-performance rotor (HPR) with an enhanced

**Fig. 9**  $C_p$  distribution at the blade suction side and pressure side



averaged torque coefficient of 48.95% with a decreased averaged efficiency of 5.56% due to dissipation effect induced by the LEM. The performance comparison between the BLR and Case F (HPR) is shown in Fig. 7h.

#### 4.4 Flow field analysis

Figure 8 illustrates the chord-wise pressure coefficient ( $C_p$ ) distribution at 50% (mid-span) and 95% (near tip) blade span for three  $U^*$  values ( $= 0.075, 0.225,$  and  $0.275$ ). The blade loading increases gradually from the mid-span to the tip region for both BLR and HPR cases. The area enclosed by the pressure distribution curve shows the work extracted by the turbine blade. When the turbine stalls, the minimum suction vanishes, and the area under the curve decreases. For  $U^* < 0.225$ , the blade loading varies marginally for both cases, which validates the  $T^*$  comparison shown in Fig. 7h. The LE suction vanishes at a higher  $U^*$  ( $= 0.275$ ), and a uniform  $C_p$  appears for the BLR case. It implies flow separation and stalls in the BLR. In contrast, the LE minimum suction increases for the HPR blade, and a higher-pressure difference between the pressure surface (PS) and SS increases the torque (Fig. 7h).

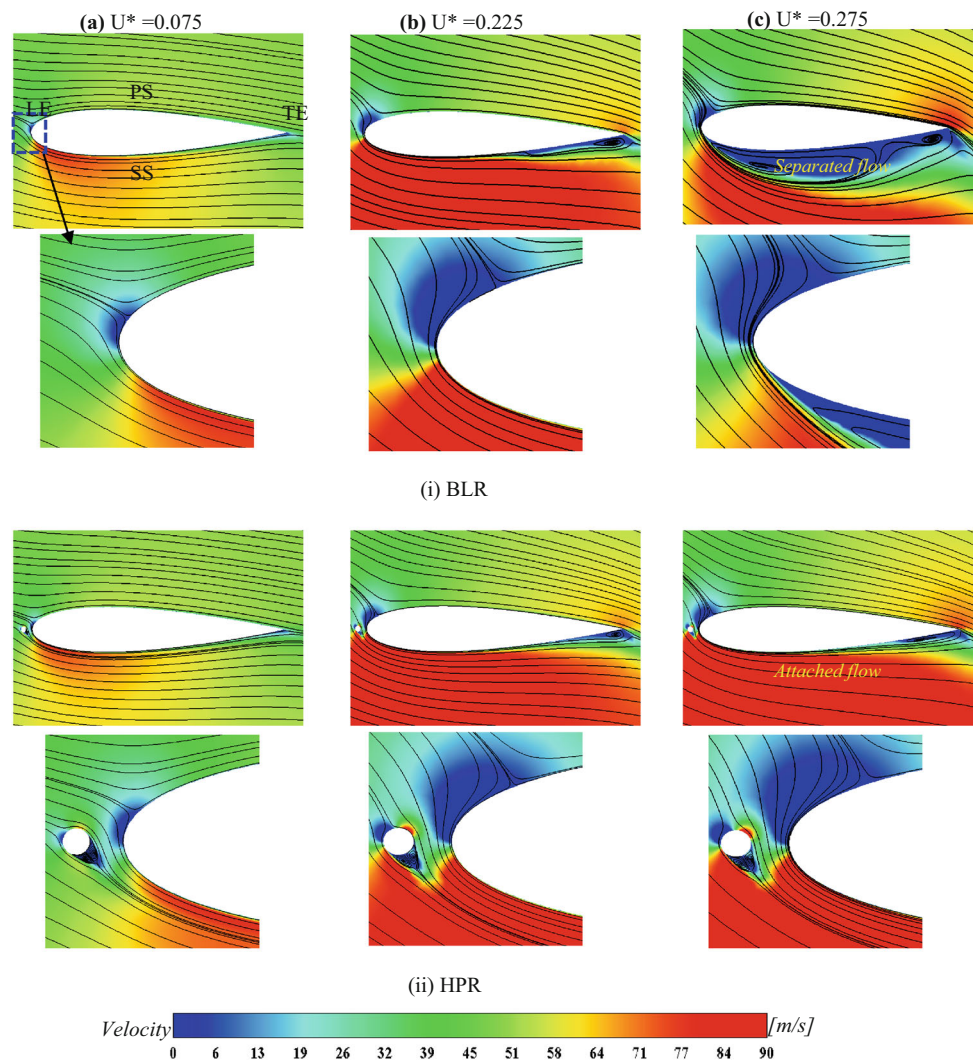
The flow is attached to the SS at a lower  $U^*$  (Fig. 9). The pressure distribution is similar for both cases for  $U^* \leq$

$0.225$ . However, for  $U^* = 0.275$ , the LE suction vanishes and the turbine stalls for the BLR. Whereas the HPR blade exhibits increased LE suction, the enhanced pressure difference across the blade improved the torque and delayed stall. The results corroborate the torque and blade loading characteristics shown in Figs. 7h and 8. The LEM enhances the pressure distribution on the SS and PS at a higher  $U^*$ . The LEM generates a vortex and transfers additional kinetic energy to prevent separation from the SS.

Figure 10 shows the velocity contours at the blade mid-span to explain the improved performance of the HPR. A lower  $U^*$  ( $= 0.075$ ) gives a fully attached flow for both cases. With a further increase in  $U^*$  ( $= 0.225$ ), the BLR displays a larger TE separation vortex than the HPR. At  $U^* = 0.275$ , the BLR blade experiences flow separation from the LE because a higher AOA and the separated flow engulf the blade SS. Alternatively, the LEM regulates the local flow direction near the blade LE for the HPR blade and eliminates the LE flow separation. It explains that the HPR blade delayed the stall and increased the operating range.

The dimensionless Z-vorticity ( $\omega_Z^*$ ) contour with streamlines at the blade mid-span is illustrated in Fig. 11. The clockwise and counter-clockwise directions indicate negative and positive vorticity. The vorticity distribution over the mid-span airfoil section shows marginal variation for

**Fig. 10** Velocity contour along with streamlines at blade mid-span



the BLR and HPR blades for  $U^* \leq 0.225$ . The LEM creates a pair of counter-rotating vortices convected downstream of the microcylinder. The vortex strength increases with an increase in  $U^*$ . At  $U^* = 0.275$ , the flow separates from LE to TE for the BLR blade, while the counter-clockwise vortex suppresses the LE flow separation by feeding kinetic energy to the boundary layer for the HPR blade. Thus, the LEM manipulates the boundary layer flow and subdues the flow separation. As a result, the LEM enhanced the operating range and torque output at  $U^* = 0.275$  (Fig. 7h). Several articles (Luo et al. 2017; Zhong et al. 2019; Geng et al. 2021) reported similar flow behavior for both steady and unsteady flow analyses.

The three most predominant turbomachinery losses are profile loss (PL), secondary flow loss (SFL) (or end wall loss), and tip leakage flow (TLF) loss (Niu and Zang 2011). The span-wise total pressure loss coefficient ( $C_{ptot}$ ) distribution at the turbo line T2 (Fig. 12) is shown in Fig. 13. At  $U^* = 0.075$ , the variation of total pressure loss is marginal for the BLR and

HPR blades. At  $U^* = 0.225$ , the profile loss and combined SFL and TLF loss are higher for the BLR than the HPR blade. An increased SFL and TLF loss implies a strong presence of the mainstream flow and TLF interaction. Furthermore, at  $U^* = 0.275$ , BLR shows a relatively increased  $C_{ptot}$  than the HPR. The HPR blade exhibits a higher  $C_{ptot}$  close to the tip, but the PL is shorter than the BLR blade. An increased profile loss signifies flow separation and stall for the BLR blade, whereas the reduced profile loss in the HPR case indicates the attached flow at the blade SS.

Figure 14 shows the  $C_{ptot}$  contours with volumetric streamline on the planes at 20%, 50%, and 80% of the span. The tip leakage vortex (TLV) increases as  $U^*$  increases. In the BLR, TLV increases until  $U^* = 0.225$  breakdowns due to strong interaction with passage flow. The HPR delays the stalling and widens the operating range with a stable TLV. Figure 14b shows a higher  $C_{ptot}$  at  $U^* = 0.225$ , a higher TLV at the tip and develops the SS's hub corner vortex (HCV).

**Fig. 11** Normalized Z-vorticity contour (streamlines only on TE and LE) in the blade mid-span

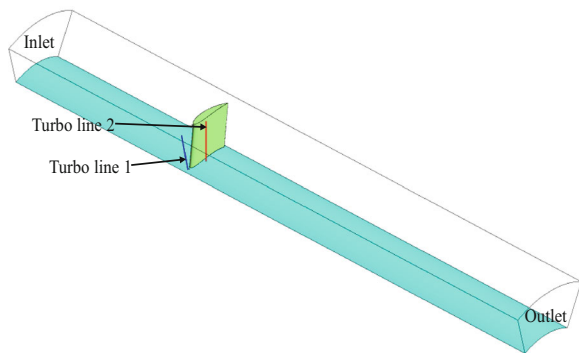
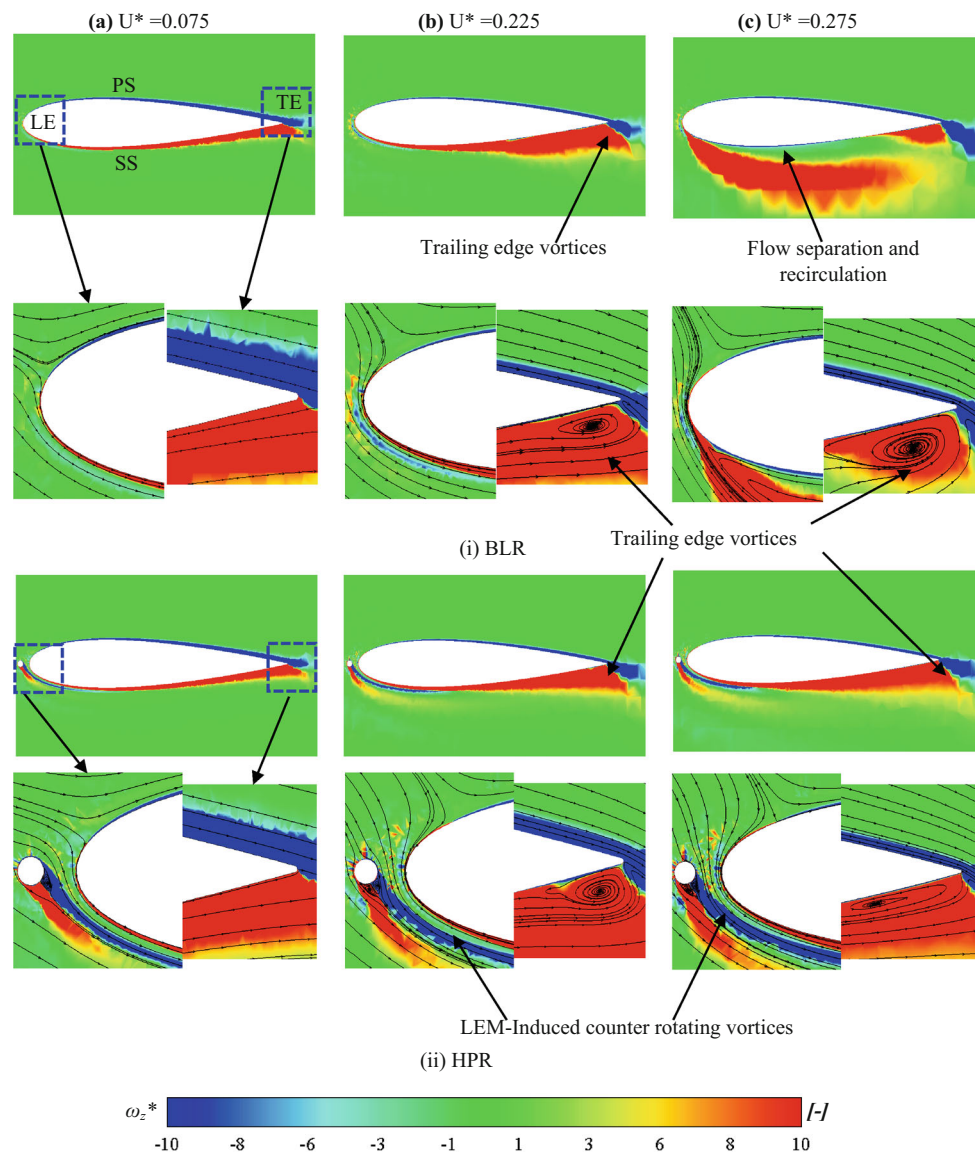


**Fig. 12** Turbo lines location at computational domain

The  $C_{p_{tot}}$  spread over the span-wise direction on the SS indicates the stall occurrence. The BLR exhibits a larger  $C_{p_{tot}}$  at  $U^* = 0.275$ , indicating flow separation on SS. Volumetric

streamlines represent the spiral form vortex tube on the BLR—SS. The HPR displays flow attachment and delays the stall at  $U^* = 0.275$ .

The skin friction coefficient contours on the SS of the rotors (with streamlines) are shown in Fig. 15. The flow is attached smoothly at  $U^*(\leq 0.225)$  in both models. At a higher  $U^*$ , the recirculation zone forms at the BLR—SS, and the streamlines show a change in the flow direction, with the flow marching span-wise direction. However, the cylinder controls the flow interaction (secondary and primary) and reduces the flow separation in the HPR—SS for  $U^* = 0.275$ .

The  $x$ -wall shear stress distribution along the mid-span (50% C) and tip (95% C) of the blade is shown in Fig. 16. At the SS, the value of  $x$ -wall shear stress is zero or negative, indicating the flow separation. The lower  $U^* (= 0.075)$  shows smooth flow attachment at the mid-span and tip. The

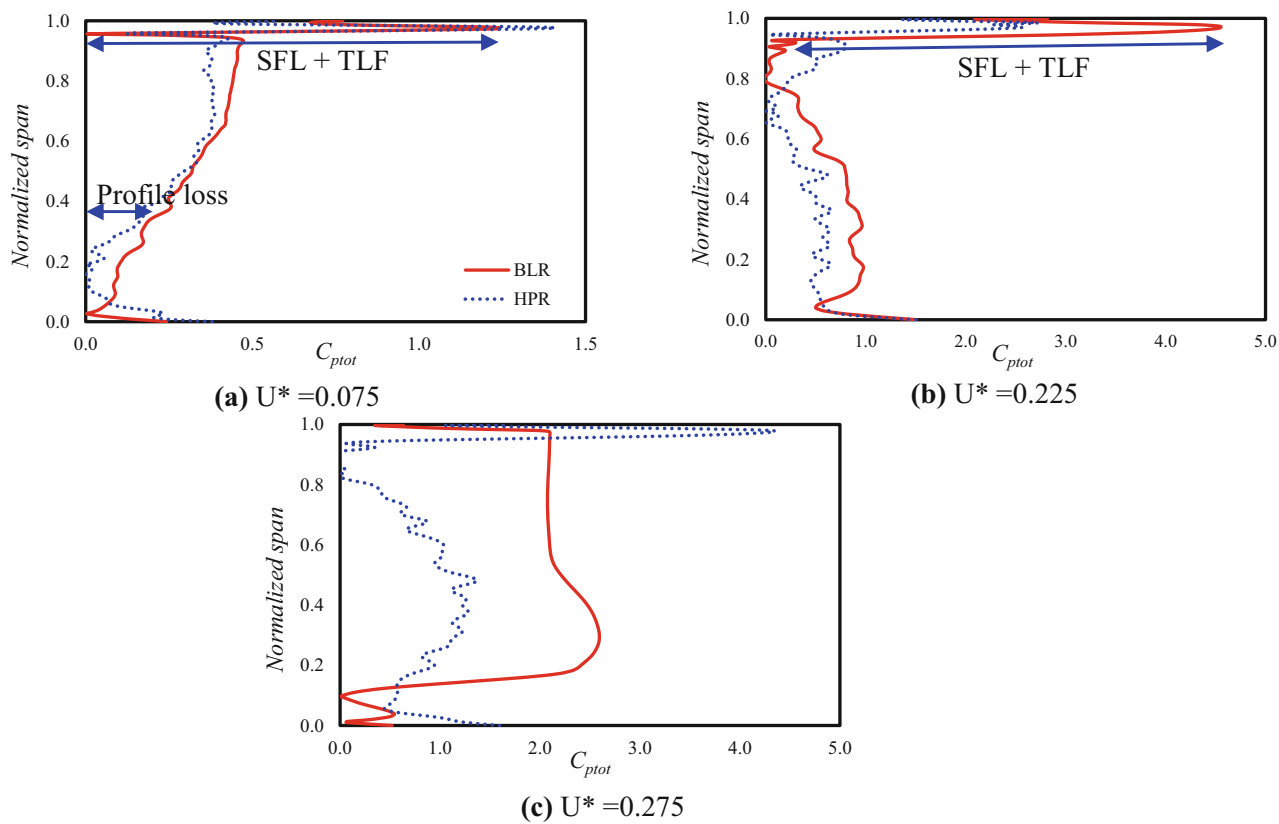
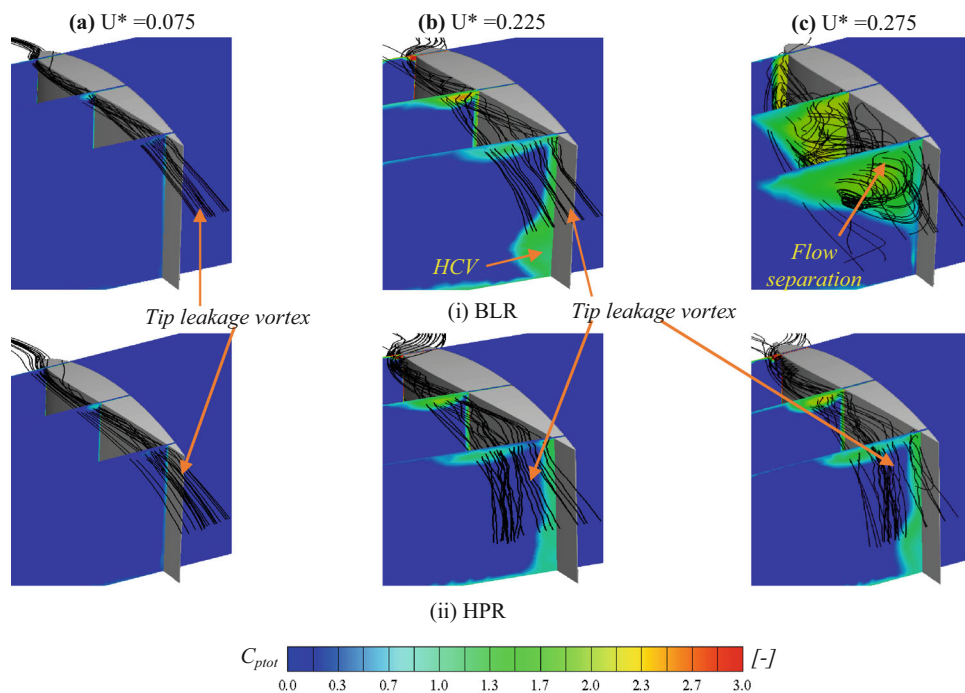
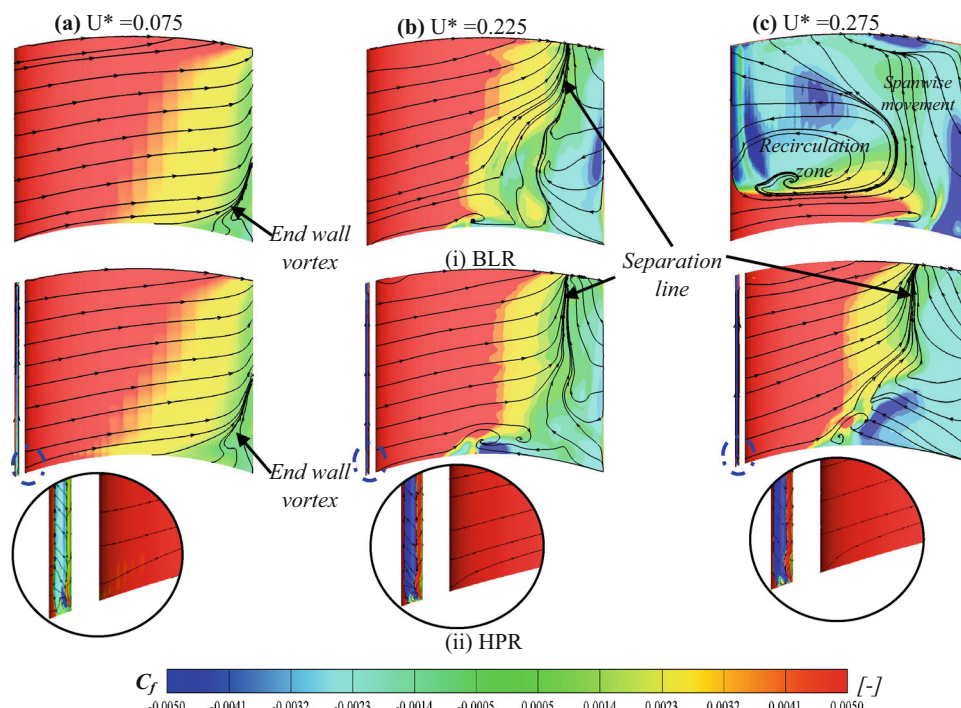


Fig. 13 Total pressure loss coefficient at blade SS for different  $U^*$  (Turbo line 2)

Fig. 14 Total pressure loss coefficient contour with volume streamlines





**Fig. 15** Contour of skin friction coefficient with SS streamlines

increasing  $U^*$  increases  $\tau_w$  (Figs. 15 and 16). The cylinder promotes the vortex close to the LE and alters the incoming flow. The flow separation occurs LE close to the HPR—LE at  $U^* = 0.275$ , but the vortex generated by the cylinder suppresses the flow separation in SS. The flow remains attached to 75–80%C of HPR mid-span and tip (Fig. 16e, f).

The non-dimensional axial velocity increases with increasing  $U^*$  (Fig. 17). As  $U^*$  increases, the axial velocity also increases. A higher axial velocity indicates a higher AOA. For  $U^* \leq 0.225$ , the span-wise axial velocity distribution for the BLR and the HPR cases show similar behavior. However, for a higher  $U^*$  ( $= 0.275$ ), the HPR blade exhibits relatively lower axial velocity near the tip region than the BLR case. The cylinder alters the axial velocity of the inward flow. As a result, the AOA in the inward flow changes and intensifies the axial velocity with an increase in  $U^*$ . This decrement in axial velocity near the tip implies reduced AOA in the tip region and can be attributed to the delayed stall.

The non-dimensional tangential velocity contour is shown in Fig. 18 for different  $U^*$  values at a plane located in the blade mid-chord. The flow is closely attached in the lower  $U^*$ , and the blade SS shows a lower strength tip leakage vortex (TLV). The end wall or hub corner vortex formed close to the blade hub portion. The TLV strength increases with  $U^*$  for both rotors. At  $U^* = 0.075$ , the variation of TLV for the BLR and HPR cases seems insignificant; however, at  $U^* = 0.225$ , the BLR blade shows stronger TLV compared to

the HPR case. It corresponds to the total pressure loss distribution shown in Fig. 12. For  $U^* \leq 0.225$ , the interaction of TLV and the primary flow is weak, and the flow blockage is minimum. With a further increase in  $U^*$  ( $= 0.275$ ), the TLF strongly interacts with the mainstream flow in the BLR blade and promotes flow separation due to increased blockage. Alternatively, the LEM in the HPR blade reduces the interaction and the flow blockage, the flow remains attached throughout the span, and the stall inception delays.

Figure 19 shows the Q-criterion colored with  $U_{tan}/U_{tip}$ . The TLV and trailing edge vortices (TEV) at the SS grow with an increase in  $U^*$ . As the  $U^*$  increases, the encounter between TLV and mainstream flow intensifies. For a lower  $U^*$  ( $= 0.075$ ), TLV strength is low, and the flow smoothly attaches for both BLR and HPR. At  $U^* = 0.275$ , the BLR presents a stronger interaction between mainstream flow and TLV, resulting in increased flow obstruction. However, the HPR blade exhibits a weaker interaction between TLF and mainstream flow that delays the stall inception. Hence, the LEM mitigates the TLV encounter with the mainstream flow and increases the operating range by delaying the stall.

## 5 Conclusion

In this work, a leading-edge microcylinder (LEM) was adopted as a flow control device for a Wells turbine to enhance its operating range. The optimum combination of

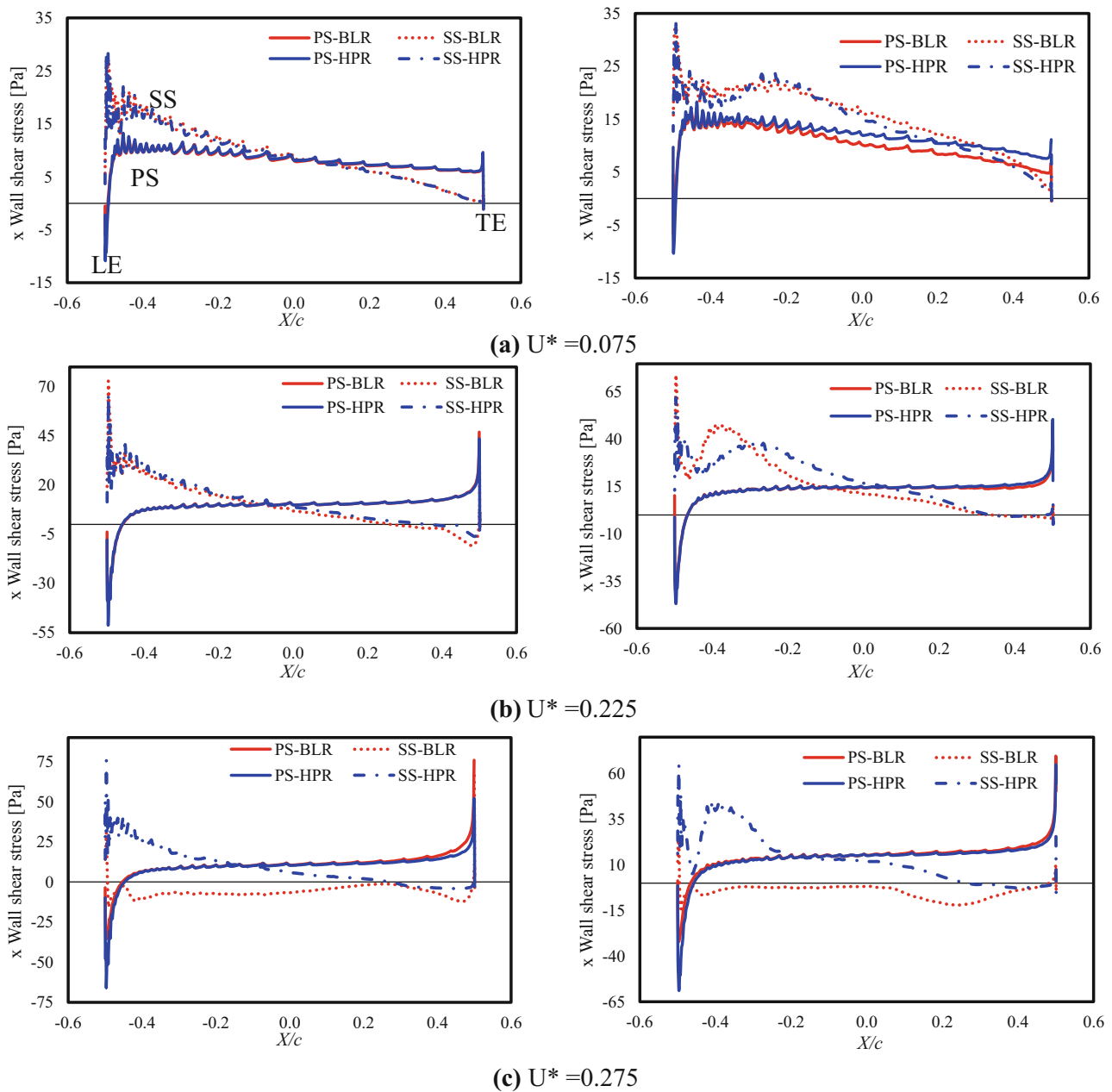


**Fig. 16** x-wall shear stress distribution on blade mid-span (left) and tip (right)

the gap ( $l$ ) and the cylinder diameter ( $d$ ) was determined through numerical analyses. The conclusions are:

- The gap ( $l$ ) and diameter ( $d$ ) are the critical parameters in delaying flow separation. The LEM blade with the appropriate combination of spacing and diameter delayed the flow separation and improved the operating range of the Wells turbine.
- The LEM blade combined with  $d = 2\%C$  and  $l = 3.5\%C$  improved the stall margin and the average torque output by 22.22% and 48.95%.
- The LEM regulated the flow direction near the blade leading edge and produced a pair of counter-rotating vortices that transmitted kinetic energy to the boundary layer and reenergized it, delaying the flow separation.
- The average efficiency of the HPR was observed to be 5.5% lesser than BLR due to the dissipation effect of LEM presence.
- A multi-objective optimization of the LEM parameters has been planned as future work to produce a high-performance Wells turbine with increased torque and operating range.

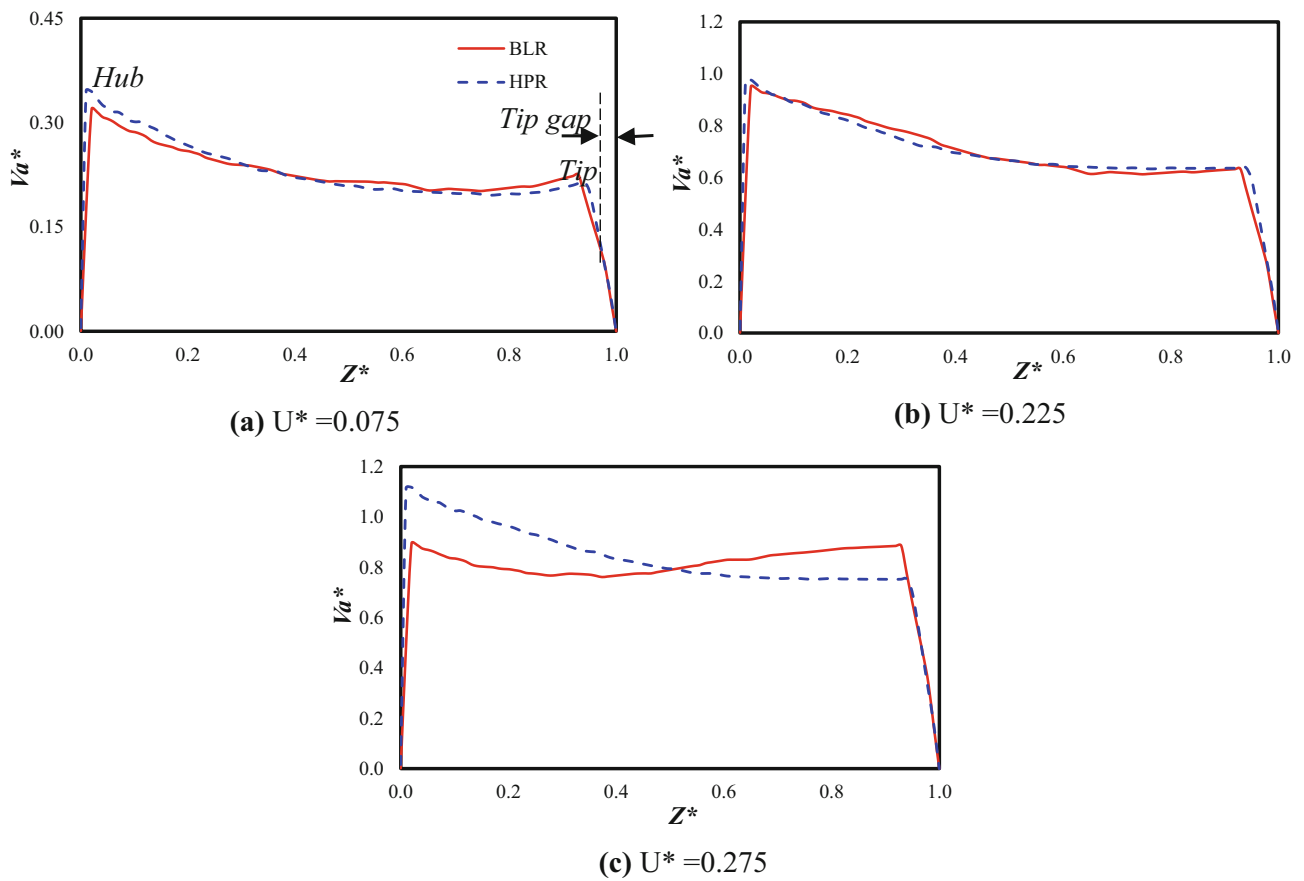
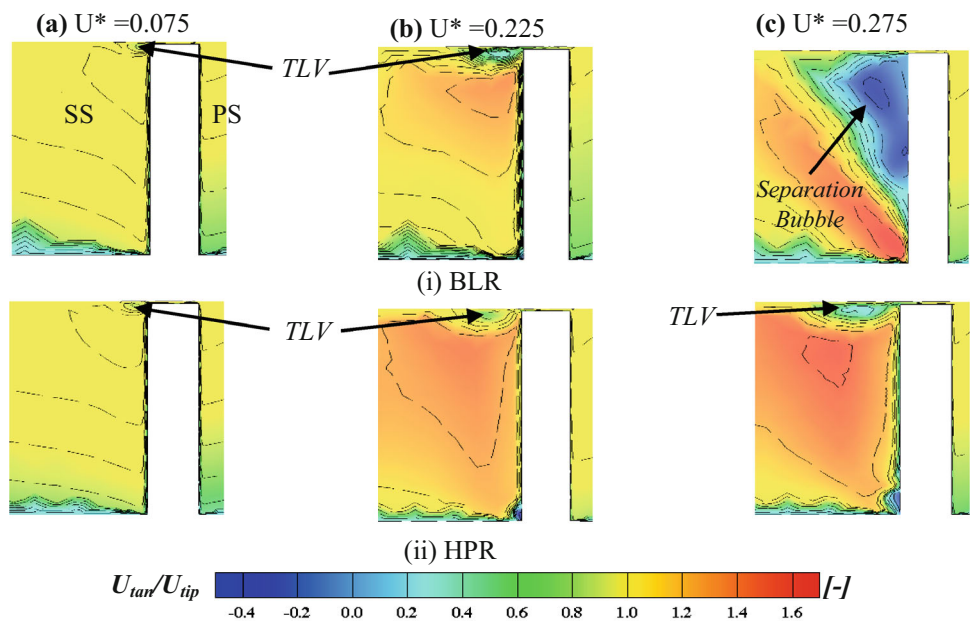


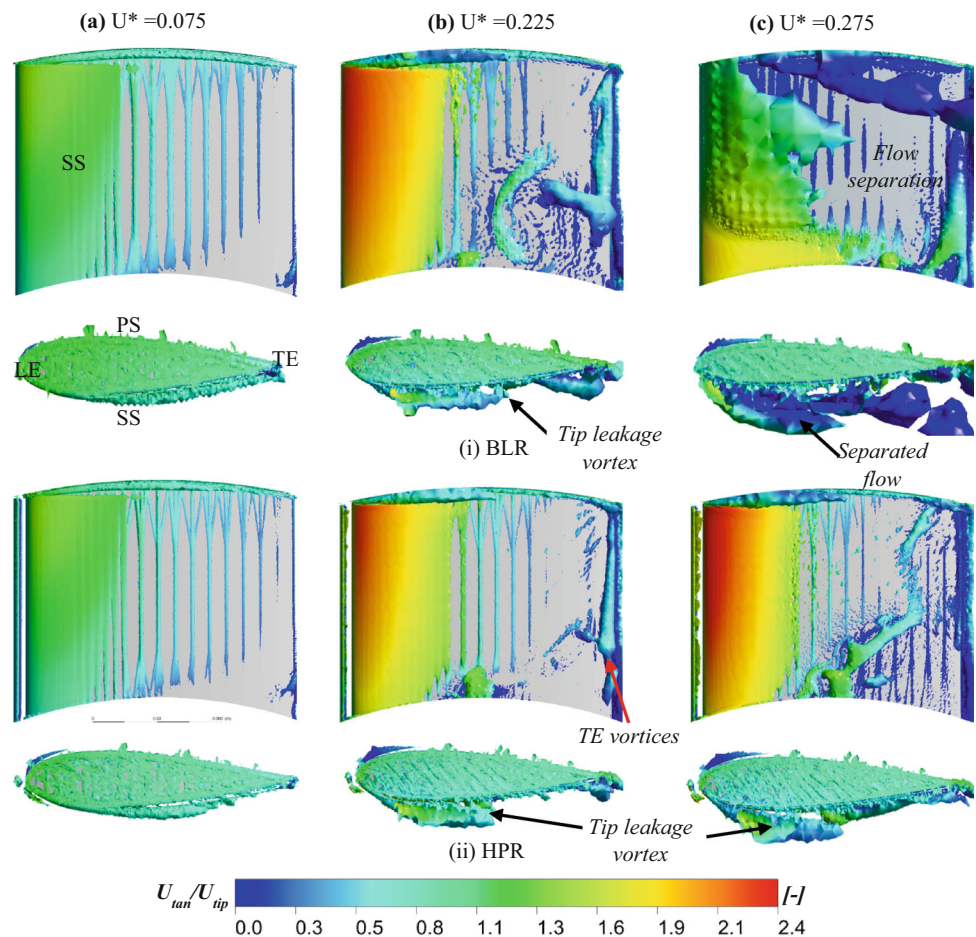
Fig. 17 Non-dimensional axial velocity distribution at TL 1

Fig. 18 Non-dimensional tangential velocity contour at mid-chord





**Fig. 19** Q-criterion value of  $5.5 \times 10^6 \text{ S}^{-2}$  colored with non-dimensional tangential velocity.



**Acknowledgements** The authors want to thank the Indian Institute of Technology Madras in Chennai, Tamil Nadu, for helping them carry out this research.

**Data availability** The data will be made available on request.

**Declarations**

**Conflict of interest** The authors have no financial or personal conflict of interest that would have seemed to impact the work described in this article.

**Appendix**

**Grid independent test**

The procedures provided in the article (Celik et al. 2008) are followed to determine the GCI. The three different mesh resolutions were adopted in this study, coarse mesh (1.17 million), medium mesh (3.53 million), and fine mesh (7.79 million). The number of elements increased based on the literature and the refinement factor value should not be lower than 1.3. To determine the GCI percentage of error in the

computational study, the average grid size was calculated by,

$$h = \left[ \frac{1}{N} \sum_{i=1}^N (\Delta Vi) \right]^{\frac{1}{3}} \tag{1}$$

where  $N$  number of mesh elements and  $\Delta Vi$  net volume of  $i$ th element. The next step is to determine the refinement factor( $r$ ). Let us consider  $h_1 < h_2 < h_3$  the subscript 1-fine, 2-medium, and 3-coarse mesh,

$$r_{21} = \frac{h_2}{h_1}, r_{32} = \frac{h_3}{h_2} \tag{2}$$

Calculate the apparent parameter ( $p$ ) used for the following expression,

$$p = \frac{1}{\ln(r_{21})} \left| \ln \left| \frac{\epsilon_{32}}{\epsilon_{21}} \right| + q(p) \right| \tag{3a}$$

$$q(p) = \ln \left\{ \frac{r_{21}^p - s}{r_{32}^p - s} \right\} \tag{3b}$$

$$s = 1.sign \left\{ \frac{\epsilon_{32}}{\epsilon_{21}} \right\} \tag{3c}$$

where  $\varepsilon_{32} = \phi_3 - \phi_2$ ,  $\varepsilon_{21} = \phi_2 - \phi_1$   $\phi_k$  –solution of the  $k$ th element. The Eq. (3a)  $q(P)$  is considered zero if the successive grid refinement factor is constant. The convergence ratio ( $R$ ) is expressed as

$$R = \left\{ \frac{\varepsilon_{32}}{\varepsilon_{21}} \right\} \quad (3d)$$

Based on the value of ‘ $R$ ’, the nature of convergence will be identified as monotonic ( $0 < R < 1$ ), oscillatory ( $0 < R$ ), and divergence ( $R > 1$ ).

Hence, the equation of the apparent parameter is expressed in Eq. (3e), and the value ‘ $p$ ’ is calculated based on the value of the critical factor ( $\phi$ ).

$$p = \frac{1}{\ln(r_{21})} \left| \ln \left| \frac{\varepsilon_{32}}{\varepsilon_{21}} \right| \right| \quad (3e)$$

Calculate the extrapolated values from the expression,

$$\phi_{ext}^{21} = \left[ \frac{r_{21}^p \phi_1 - \phi_2}{r_{21}^p - 1} \right] \quad (4a)$$

The approximate and extrapolated relative errors are calculated from,

$$e_a^{21} = \left| \frac{\phi_1 - \phi_2}{\phi_1} \right| \quad (5)$$

$$e_{ext}^{32} = \left| \frac{\phi_{ext}^{32} - \phi_3}{\phi_{ext}^{32}} \right| \quad (6)$$

where subscript  $a$  and  $ext$  denote the approximate error and extrapolated error. The fine  $GCI$  is calculated from the expression of the following

$$GCI_{fine}^{21} = \left( \frac{1.25e_a^{21}}{r_{21}^p - 1} \right) \quad (7)$$

## References

ANSYS-CFX (2011) ANSYS CFX-solver modeling guide

Beyhaghi S, Amano RS (2017) Improvement of aerodynamic performance of cambered airfoils using leading-edge slots. *J Energy Resour Technol Trans ASME* 139:1–8. <https://doi.org/10.1115/1.4036047>

- Buchmann NA, Atkinson C, Soria J (2013) Influence of ZNMF jet flow control on the spatio-temporal flow structure over a NACA-0015 airfoil. *Exp Fluids*. <https://doi.org/10.1007/s00348-013-1485-7>
- Cai C, Liu S, Zuo Z et al (2019) Experimental and theoretical investigations on the effect of a single leading-edge protuberance on airfoil performance. *Phys Fluids* 31:027103. <https://doi.org/10.1063/1.5082840>
- Celik IB, Ghia U, Roache PJ et al (2008) Procedure for estimation and reporting of uncertainty due to discretization in CFD applications. *J Fluids Eng Trans ASME* 130:0780011–0780014. <https://doi.org/10.1115/1.2960953>
- Cui Y, Hyun BS (2016) Numerical study on Wells turbine with penetrating blade tip treatments for wave energy conversion. *Int J Nav Archit Ocean Eng* 8:456–465. <https://doi.org/10.1016/j.ijnaoe.2016.05.009>
- Curran R, Gato LMC (1997) The energy conversion performance of several types of Wells turbine designs. *Proc Inst Mech Eng Part A J Power Energy* 211:133–145. <https://doi.org/10.1243/0957650971537051>
- Das TK, Samad A (2020) Influence of stall fences on the performance of Wells turbine. *Energy* 194:116864. <https://doi.org/10.1016/j.energy.2019.116864>
- Donovan JF, Kral LD, Gary AW (1998) Active flow control applied to an airfoil. 36th AIAA Aerosp Sci Meet Exhib. Doi: <https://doi.org/10.2514/6.1998-210>
- Falcao A (2010) Wave energy utilization: a review of the technologies. *Renew Sustain Energy Rev* 14:899–918. <https://doi.org/10.1016/j.rser.2009.11.003>
- Geng K, Yang C, Hu C et al (2021) Performance investigation of Wells turbine for wave energy conversion with stall cylinders. *Ocean Eng* 241:110052. <https://doi.org/10.1016/j.oceaneng.2021.110052>
- Ghisu T, Puddu P, Cambuli F (2015) Numerical analysis of a wells turbine at different non-dimensional piston frequencies. *J Therm Sci* 24:535–543. <https://doi.org/10.1007/s11630-015-0819-6>
- Ghisu T, Puddu P, Cambuli F (2016) Physical explanation of the hysteresis in wells turbines: a critical reconsideration. *J Fluids Eng Trans ASME* 138:1–9. <https://doi.org/10.1115/1.4033320>
- Ghisu T, Puddu P, Cambuli F (2017) A detailed analysis of the unsteady flow within a Wells turbine. *Proc Inst Mech Eng Part A J Power Energy* 231:197–214. <https://doi.org/10.1177/0957650917691640>
- Gopalkrishnan R, Triantafyllou MS, Triantafyllou GS, Barrett D (1994) Active vorticity control in a shear flow using a flapping foil. *J Fluid Mech* 274:1–21. <https://doi.org/10.1017/S0022112094002016>
- Greenblatt D, Pfeffermann O, Keisar D, Göksel B (2021) Wells turbine stall control using plasma actuators. *AIAA J* 59:765–772. <https://doi.org/10.2514/1.J060278>
- Halder P, Samad A, Kim JH, Choi YS (2015) High performance ocean energy harvesting turbine design-A new casing treatment scheme. *Energy* 86:219–231. <https://doi.org/10.1016/j.energy.2015.03.131>
- Halder P, Samad A, Thévenin D (2017) Improved design of a Wells turbine for higher operating range. *Renew Energy* 106:122–134. <https://doi.org/10.1016/j.renene.2017.01.012>
- Hansen KL, Kelso RM, Dally BB (2011) Performance variations of leading-edge tubercles for distinct airfoil profiles. *AIAA J* 49:185–194. <https://doi.org/10.2514/1.J050631>
- Jacob MC, Boudet J, Casalino D, Michard M (2005) A rod-airfoil experiment as a benchmark for broadband noise modeling. *Theor Comput Fluid Dyn* 19:171–196. <https://doi.org/10.1007/s00162-004-0108-6>
- Kumar KN, Govardhan M (2011) Secondary flow loss reduction in a turbine cascade with a linearly varied height streamwise endwall fence. *Int J Rotating Mach* 2011:1–16. <https://doi.org/10.1155/2011/352819>
- Kumar PM, Halder P, Samad A, Rhee SH (2018) Wave energy harvesting turbine: effect of hub-to-tip profile modification. *Int J*

- Fluid Mach Syst 11:55–62. <https://doi.org/10.5293/IJFMS.2018.11.1.055>
- Kumar PM, Halder P, Samad A (2021) Radiused edge blade tip for a wider operating range in wells turbine. Arab J Sci Eng 46:2663–2676. <https://doi.org/10.1007/s13369-020-05185-z>
- Luo D, Huang D, Sun X (2017) Passive flow control of a stalled airfoil using a microcylinder. J Wind Eng Ind Aerodyn 170:256–273. <https://doi.org/10.1016/j.jweia.2017.08.020>
- Mai H, Dietz G, Geißler W et al (2008) Dynamic stall control by leading edge vortex generators. J Am Helicopter Soc 53:26. <https://doi.org/10.4050/JAHS.53.26>
- Menter FR (1994) Two-equation eddy-viscosity turbulence models for engineering applications. AIAA J 32:1598–1605. <https://doi.org/10.2514/3.12149>
- Mostafa W, Abdelsamie A, Sedrak M et al (2022) Quantitative impact of a micro-cylinder as a passive flow control on a horizontal axis wind turbine performance. Energy 244:122654. <https://doi.org/10.1016/j.energy.2021.122654>
- Nazeryan M, Lakzian E (2018) Detailed entropy generation analysis of a Wells turbine using the variation of the blade thickness. Energy 143:385–405. <https://doi.org/10.1016/j.energy.2017.11.006>
- Niu M, Zang S (2011) Experimental and numerical investigations of tip injection on tip clearance flow in an axial turbine cascade. Exp Therm Fluid Sci 35:1214–1222. <https://doi.org/10.1016/j.expthermflusci.2011.04.009>
- Raghunathan S (1995) The Wells air turbine for wave energy conversion. Prog Aerosp Sci 31:335–386. [https://doi.org/10.1016/0376-0421\(95\)00001-F](https://doi.org/10.1016/0376-0421(95)00001-F)
- Sadees P, Kumar PM, Samad A (2021) Effect of microcylinder and D-cylinder at the leading edge of a wells turbine harvesting wave energy. In: Volume 2B: Turbomachinery—Axial Flow Turbine Aerodynamics; Deposition, Erosion, Fouling, and Icing. American Society of Mechanical Engineers, pp 1–8
- Shaaban S, Hafiz AA (2012) Effect of duct geometry on Wells turbine performance. Energy Convers Manag 61:51–58. <https://doi.org/10.1016/j.enconman.2012.03.023>
- Shalby M, Dorrell DG, Walker P (2019) Multi-chamber oscillating water column wave energy converters and air turbines: a review. Int J Energy Res 43:681–696. <https://doi.org/10.1002/er.4222>
- Shehata AS, Xiao Q, Saqr KM, Alexander D (2017a) Wells turbine for wave energy conversion: a review. Int J Energy Res 41:6–38. <https://doi.org/10.1002/er.3583>
- Shehata AS, Xiao Q, Selim MM et al (2017b) Enhancement of performance of wave turbine during stall using passive flow control: first and second law analysis. Renew Energy 113:369–392. <https://doi.org/10.1016/j.renene.2017.06.008>
- Stough HP, Jordan FL, Dicarolo DJ, Glover KE (1985) Leading-edge design for improved spin resistance of wings incorporating conventional and advanced airfoils. SAE Tech Pap 94:502–516. <https://doi.org/10.4271/851816>
- Strüber H, Wild J (2014) Aerodynamic design of a high-lift system compatible with a natural laminar flow wing within the desireh project. 29th Congr Int Counc Aeronaut Sci ICAS 2014 1–8
- Taha Z, Sugiyono TYTS, Sawada T (2011) Numerical investigation on the performance of Wells turbine with non-uniform tip clearance for wave energy conversion. Appl Ocean Res 33:321–331. <https://doi.org/10.1016/j.apor.2011.07.002>
- Takao M, Setoguchi T, Inoue M (2000) The performance of wells turbine with 3D guide vanes. Proc Tenth Int Offshore Polar Eng Conf Seattle 1:381–386
- Torresi M, Camporeale SM, Strippoli PD, Pascazio G (2008) Accurate numerical simulation of a high solidity Wells turbine. Renew Energy 33:735–747. <https://doi.org/10.1016/j.renene.2007.04.006>
- Torresi M, Camporeale SM, Pascazio G, Fortunato B (2004) Fluid dynamic analysis of a low solidity wells turbine. 59° Congr ATI, Genova Italy 2004:
- Wang Y, Li G, Shen S et al (2018) Investigation on aerodynamic performance of horizontal axis wind turbine by setting micro-cylinder in front of the blade leading edge. Energy 143:1107–1124. <https://doi.org/10.1016/j.energy.2017.10.094>
- Watterson JK, Raghunathan S (1997) Computed effects of tip clearance on wells turbine performance. 35th Aerosp Sci Meet Exhib 1–9. <https://doi.org/10.2514/6.1997-994>
- Yahiaoui T, Belhenniche M, Imine B (2015) Effect of moving surface on NACA 63218 aerodynamic performance. EPJ Web Conf 92:1–4. <https://doi.org/10.1051/epjconf/20159202114>
- Zhong J, Li J, Guo P, Wang Y (2019) Dynamic stall control on a vertical axis wind turbine aerofoil using leading-edge rod. Energy 174:246–260. <https://doi.org/10.1016/j.energy.2019.02.176>

**Publisher's Note** Springer Nature remains neutral with regard to jurisdictional claims in published maps and institutional affiliations.

Springer Nature or its licensor (e.g. a society or other partner) holds exclusive rights to this article under a publishing agreement with the author(s) or other rightsholder(s); author self-archiving of the accepted manuscript version of this article is solely governed by the terms of such publishing agreement and applicable law.